Ocean Engineering 235 (2021) 109426

Contents lists available at ScienceDirect

Ocean Engineering

journal homepage: www.elsevier.com/locate/oceaneng

Multipurpose breakwater: Hydrodynamic analysis of flap-type wave energy converter array integrated to a breakwater

Saghy Saeidtehrani [a,*], Madjid Karimirad [b]

[a] OBS Consulting Engineers, Tehran, Iran
[b] School of Natural and Built Environment, Queen's University Belfast, UK

ARTICLE INFO

Keywords:
Wave energy converter
Numerical simulation
Nonlinear dynamic analysis
Wave-structure interaction
Multipurpose breakwater

ABSTRACT

Wave Energy Converter (WEC) development needs a thorough dynamic characterization of the device and tuning the design properties to harness the maximum power. This paper addresses this need by using experimentally validated numerical simulation for an array of flap-type WEC mounted on a surface of a breakwater as a coherent approach in sustainable coastal protection. The developed numerical model is combined with a parametric iteration procedure to find the optimized values of power take-off (PTO) coefficients, and the flap's distance from the breakwater. It is shown that tuning the design properties of flap-type WEC integrated into a coastal structure leads to high energy capture around 85 percent of the available power. It was found that the amplitude of oscillation is significantly affected by the presence of different frequencies resultant from standing waves, and the confined water between the flap and the breakwater. It turns out that by tuning the distance between the flap and the breakwater, the standing waves can be used for increasing the amplitude of oscillation and consequently power enhancement.

1. Introduction

There are plenty of Wave Energy Converter (WEC) concepts with unique functionality that are developed for specific environmental loads. WEC concepts are mainly classified based on location, working principle, and size (López et al., 2013). From the operational aspect, the WECs are further categorized as oscillating water columns, overtopping devices, and wave-activated bodies (Czech and Bauer, 2012). The later concept harnesses energy by wave-induced motion of the submerged or floating structures (Qiao et al., 2020).

Representing the realistic performance of WECs is an important step in increasing the efficiency and economic viability of the device that can be achieved by developing reliable simulation tools which in turn is a challenging process due to the diversity of the concepts (Karimirad, 2014a), and the consequent numerical requirements (Ruehl et al., 2020).

The focus of this paper is on flap-type WEC, a wave-activated body (Qiao et al., 2020), that is considered as an efficient device with larger frequency bandwidth (Babarit et al., 2012; Todalshaug, 2017) among various WEC concepts (Falcão, 2010; Uihlein and Magagna, 2016). Normally, devices with reasonable body size don't have large bandwidth, and wider frequency bandwidth can be achieved by tuning the device with the wave conditions to produce resonance (Falnes, 2007).

Tuning device characteristics can be combined with the idea of using multipurpose coastal structures to increase the frequency bandwidth and consequently enhancing the efficient operation (Zhao et al., 2019) which is the opportunity-focused mindset on the functionality of the WEC devices and utilizing the existent coastal structures. This strategy is aligned with the sustainable coastal protection and the mutual benefits of WEC devices and coastal areas (Mendoza et al., 2014; Zanuttigh and Angelelli, 2013). The concept of the multipurpose breakwater is presented for different WEC concepts from oscillating WECs (Sammarco et al., 2015) to oscillating water columns (Rosa-Santos et al., 2019).

Multipurpose structures not only decrease the shared costs but, in some cases, their presence increases the frequency bandwidth of the WEC device. However, the challenge of survivability and reliability to withstand huge storms as is expected from a defence structure remains. Another important part of commercialization is the proven survivability to decrease the risk of failure and expand the operational time (Greaves and Iglesias, 2018). This paper presents the first development stages of the flap-type WEC integrated into the breakwater according to the

* Corresponding author.
E-mail address: saghy.saeidt@gmail.com (S. Saeidtehrani).

https://doi.org/10.1016/j.oceaneng.2021.109426
Received 23 March 2021; Received in revised form 27 June 2021; Accepted 28 June 2021
Available online 9 July 2021

development stages (Pecher and Costello, 2017); therefore, the study is dedicated to increasing the hydrodynamic efficiency through the external geometry and the PTO coefficients.

To increase the efficiency of the flap-type WEC integrated into the breakwater, some linear semi-analytical studies for the enhancement of exciting torque and tunning wall distance with the natural modes are conducted (Michele et al., 2016). This topic was also investigated by experimental tests and it was shown that there is some kind of instability in the flap behaviour due to the formation of antinodes when the ratio of wall distance to wavelength approaches 0.5 (Cho et al., 2020). For overtopping WECs, it is also reported that less distance increases the amount of wave overtopping (Di Lauro et al., 2020a) which is equivalent to the wave height rise.

The goal of this paper is to provide a thorough understanding of different wave-structure phenomena affecting the behaviour of flap-type WECs mounted on the horizontal surface of the multipurpose breakwater. The presence of the breakwater changes the surrounding hydrodynamic which not only affects the wave reflection and the wave force (Di Lauro et al., 2020b) but also influences the dynamic characteristics such as mass, stiffness, and damping defining the flap-type WEC's movements.

Through this paper, the complexity involves due to the confined water between the flaps and the breakwater, the formation of standing waves or group waves, and their effects on the dynamic response are theoretically and numerically investigated. It is also responded how the whole system should be tuned to increase the power absorbance by optimization of design properties such as PTO coefficients, and the location for mounting the flap WECs. Since computationally demanding tools cannot be always a good solution, especially during the operation procedure, this paper develops 2-D models for various phases of optimization with a detailed description of its capabilities and limitations for this specific device. Later, the 3-D simulation shows that 2-D can effectively represent the flap's behaviour due to the similarity of the dynamic characteristics and the flaps' tendency to move together with a negligible phase difference (Saeidtehrani, 2015).

The organization of this paper to provide an investigation on design properties of flap WEC integrated to a breakwater is as follows: brief characterization of the device and site specification is provided in Section 2. Development of the mathematical formulation needs some understanding of the wave-body interaction which is the subject of Section 3.1. The development of a fairly accurate numerical model (Section 3.2) relies on the sensitivity analyses and the verification of the numerical tool with experimental tests that are presented in Sections 3.3 and 3.4. Design properties of the flap WEC such as PTO coefficients and the distance of the flaps from the breakwater are parametrically studied and optimized with a 2-D numerical model in Sections 4.1 and 4.2. The results are used for further 3-D investigation in Section 4.3, which proves the validity of the 2-D simulation and shows that the 2-D results can be effectively used for providing a benchmark for the design and analysis procedure. Finally, it is shown that by using the optimized values for PTO and the distance from the wall, high energy around 85 percent of the available power can be captured; other conclusions are drawn in Section 5.

2. Site description, proposed device structure, and geometry

This study is focused on a nearshore flap-type WEC composed of five flaps hinged to the seaward horizontal surface of a vertical breakwater as it was patented and proposed for the port of Piombino in Southern Tuscany (Sammarco et al., 2015). The power matrix (Paolo Sammarco et al., 2016), an area with maximum energy, and the depth contours of the port of Piombino (Navionics, 2021) are shown in Fig. 1.

The wave characteristics with $T_P \in [3.5\ 6.3]$ s and $H_s = 2$ m that has the maximum energy potential and the water depth of 12 m as a feasible place for the device installation has been chosen for this study; see (Sammarco et al., 2015) and the depth contours around the port presented in Fig. 1.

Fig. 2 shows the 1:40 scale model of the device proposed for the port of Piombino (Sammarco et al., 2015) which was the subject of preliminary physical and numerical simulation (Saeidtehrani, 2015). The water depth for the 1:40 scale model was estimated equal to 300 mm in front of the breakwater in which, at the rest position of the flaps, 50 mm of their height were underwater. Detailed information about the numerical simulation and the experimental tests is provided in the following sections.

3. Development of the numerical model

The flap-type WEC is a nonlinear oscillating system (Saeidtehrani, 2015) and is proposed to act with resonance and consequently experience rapid motions (Saeidtehrani, 2015; Sammarco et al., 1997). For developing the numerical simulation representing its nonlinear dynamic

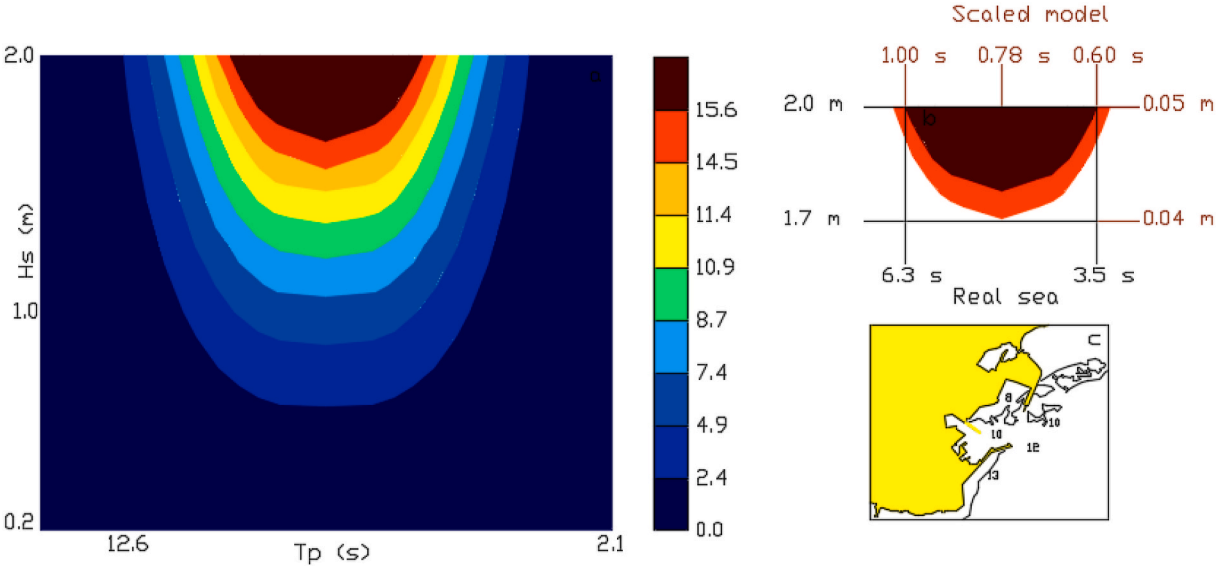

Fig. 1. a) Schematic Power Matrix inspired by (Paolo Sammarco et al., 2016); b) Area with maximum energy potential; c) Schematic depth contours inspired by (Navionics, 2021).

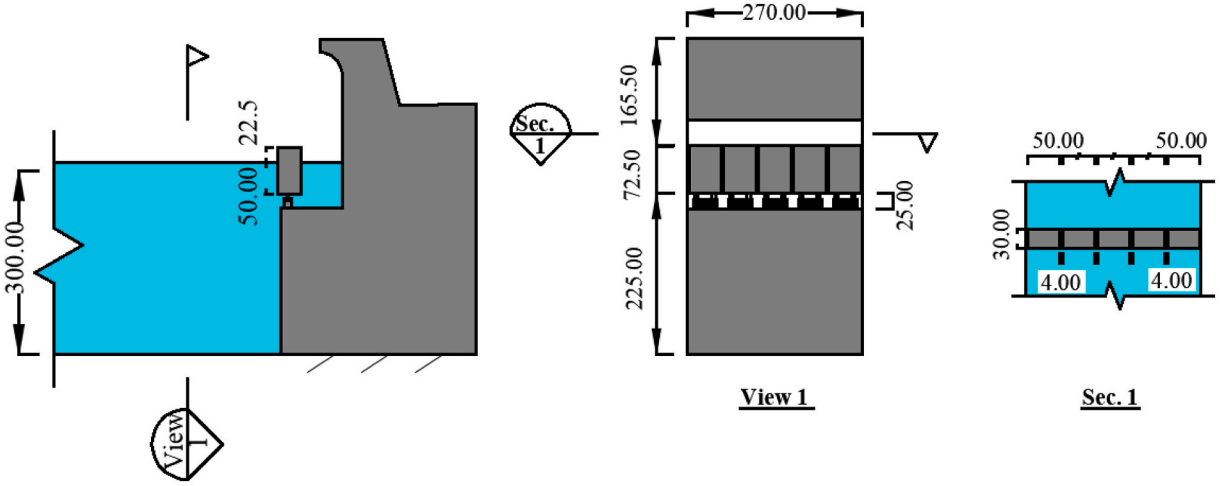

Fig. 2. Schematic view of small-scale physical model, geometry and dimensions.

behaviour, several factors should be considered including the efficiency for iterative optimization procedure, and the required fidelity to represent the fundamental wave-structure interaction affecting the WEC behaviour (Josh and Ronan, 2020).

The high fidelity of the solver is obtained by a fully nonlinear model and it is generally known that the nonlinear mathematical descriptions could best approximate the nonlinear behaviour (W.F. Ames, 1965); however, it is possible to reduce the nonlinearity and reasonably use linear assumptions to decrease the computational time and cost. Various methods combine linear and nonlinear to approach a physical problem by ignoring higher order terms or simplification in boundary conditions (Ma, 2010). For the development of the numerical simulation, first, the fundamentals of a preliminary study on wave-body interaction are presented, then the assumptions, methodology, and the approach used for developing a numerical simulation tool for the flap-type WEC integrated into breakwater is described in Section 3.2.

3.1. Preliminary study on wave-body interaction

Developing a robust while efficient numerical modelling tool for predicting the device behaviour needs a good understanding of the wave-body interaction. The wave-body interaction and the amount of perturbated or absorbed energy in the fluid are directly related to the ratio of body dimensions to the wave characteristics. Fig. 3 summarizes wave-body interaction parameters such as diffraction parameters, Keulegan–Carpenter number, and wave breaking indexes. The above-mentioned parameters are calculated based on the analytical formula provided in (Mei et al., 2005) for the flap oscillating body and in response to the wave characteristics with maximum energy potential (see Section 2). The parameters are compared with the values presented in the literature to study the importance of diffraction, drag effects, and wave breaking.

The calculated parameters are tabulated in Fig. 3- a; Fig. 3- b shows the wave characteristics, water depth, and device dimensions required

1	2	3	4	5	6	7	8	9	10	11	12
A	a	T	L	K	c	K_c	$\frac{A}{a}$	Ka	$\frac{d}{L}$	$\frac{H}{L}$	$\left(\frac{H}{L}\right)_{max}$
0.025	0.045	0.60	0.56	11.23	0.93	3.49	0.56	0.51	0.54	0.09	0.14
0.025	0.045	0.70	0.75	8.38	1.07	3.49	0.56	0.38	0.40	0.07	0.14
0.025	0.045	0.80	0.95	6.61	1.19	3.49	0.56	0.30	0.32	0.05	0.14
0.025	0.045	0.90	1.16	5.44	1.28	3.49	0.56	0.24	0.26	0.04	0.13
0.025	0.045	1.00	1.36	4.63	1.36	3.49	0.56	0.21	0.22	0.04	0.13

(a)

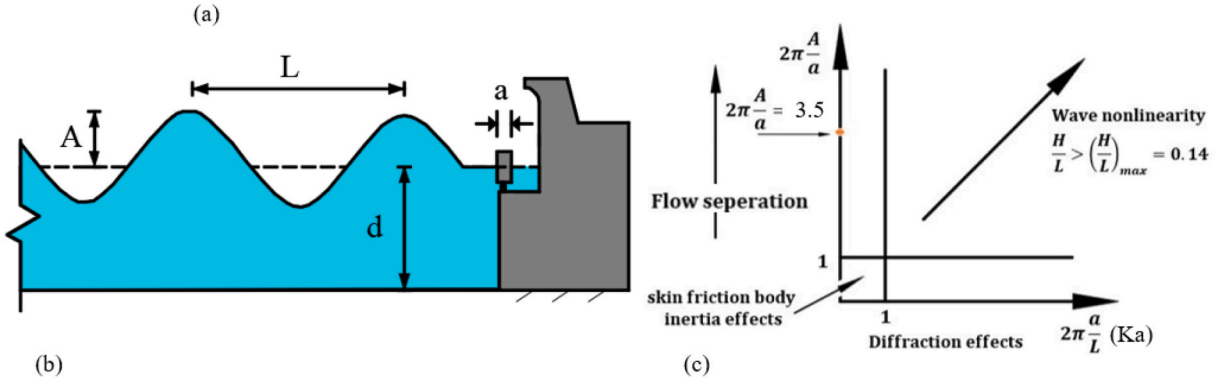

Fig. 3. a) Wave-body interaction parameters; b) Schematic view of the device and the illustrated wave characteristics, water depth, and device dimension; c) Illustrated summary of the wave-body interaction parameters inspired by (MIT, 2005).

for the calculation of wave-body interaction parameters. Fig. 3- c is inspired by (MIT, 2005) and is provided to make a clear picture of the parameters and their effects. Wave amplitude, flap width, wave period, wavelength, wavenumber, and celerity are denoted with A, a, T, L, K, c respectively in Columns 1 to 6.

Keulegan–Carpenter number (K_c) which is equal to UT/a is used for testifying the water motion relative to the floating body dimension (Column 7). U is maximum horizontal particle velocity and is equal to $2\pi A$, indicates the relation of K_c to A/a (Sorensen, 2006), the ratio of wave amplitude to floater size along with wave direction (Column 8). (A/a) provides instant anticipation of flow separation and viscous effects, and by increasing this ratio, the flow separation becomes more dominant.

From the parameters calculated for this specific project in Fig. 3- a, it can be seen that K_c is sufficiently large, and by increasing K_c more than 1, it is expected that the flow separation happens and the viscous forces cannot be neglected (see Fig. 3- c). It should be noted that large K_c number signifies large motion of water particle in comparison to the characteristic body dimension which is followed by separation and consequent vortex shedding (Juilfs, 2006; Mei et al., 2005).

a/L is recognized as a diffraction parameter, and Ka (Column 9) is the dimensionless measure to show the scattered waves by the presence of the body. Wave diffraction spreads energy in other directions than the wave propagates (Dean and Dalrymple, 1984). Parameter Ka indicates that for a wave period in the range of 0.6 s to 1.0 s, the device cannot produce any change in the wave pattern or make diffraction. As can be observed in Fig. 3- c, by increasing the diffraction parameter more than 1, the diffraction effects become significant.

Parameter d/L (Column 10) is used for categorizing the wave-bottom interaction as deep, intermediate, or shallow waves (Sorensen, 2006). For $d/L > 0.5$, the wave characteristics are not related to the depth and the wave-bottom interaction can be neglected and the assumption of deep water is correct. As can be seen in Fig. 3 and considering the limitation of d/L, the transitional or intermediate water assumption should be used for all waves except for wave periods equal to 0.6 s which should be considered as a deep-water condition (Kamphuis, 2010).

Wave breaking is one of the notable physical processes in nearshore hydrodynamics. For the nearshore operation of flap-type WEC, the possibility of wave breaking must be considered in the feasibility study to find a suitable place for the device, since waves are losing and dissipating a huge amount of energy when they break (Svendsen, 2006).

For estimating the highest possible non-breaking wave, two wave-breaking criteria are estimated here. Given the wave height of 50 mm and water depth equal to 300 mm, the ratio of wave height to depth in front of the breakwater is 0.17 which is far away from the value of 0.8261 suggested by Longuet-Higgins and Fenton, one of the accurate values for breaking index (Svendsen, 2006). This ratio physically imposed the condition for the maximum possible wave height that can be formed in the constant depth.

The ratio of wave height to wavelength (Column 11) is another parameter for recognizing breaking and non-breaking waves which is compared with the maximum steepness H/L (Column 12) estimated from the Miche equation (Svendsen, 2006). As can be observed, for all the wave periods, the steepness is less than the maximum value $(H/L)_{max} = 0.14$, thus the waves propagate without breaking. After a preliminary study on wave-body interaction, the mathematical description is developed which will be illustrated in the following section.

3.2. Theory and mathematical background

This section outlines the development of an idealized device model under the action of wave loads. For each step of the process, the parameters and assumptions are listed and described in detail. For developing the mathematical model of the flap-type WEC device, the summarized matrix form of the conservation of linear and angular momentum equations is used, then it was rewritten for one degree of freedom, pitch motion (E. Renzi, A. Abdolali and Dias, 2012). The pressure (P) on the body is substituted by the linearized first order Bernoulli equation (Svendsen, 2006). The equation describing the motion of flap is further developed to consider the linear and nonlinear damping terms and PTO effects:

$$I\ddot{\theta} + K_H\theta + K_P\theta + C_P\dot{\theta} + C_F\dot{\theta} + C_{QD1}\dot{\theta}|\dot{\theta}|(\theta \geq 1) + C_{QD2}\dot{\theta}|\dot{\theta}|(\theta < 1) = -\rho \int_{-h_r}^{0} \times \int_{-\frac{w}{2}}^{\frac{w}{2}} \phi_t(n_x(z-h_r) + n_z x)dydz \tag{1}$$

Equation (1) simply describes the equilibrium of the external load and three main forces: stiffness, damping, and inertia as a function of displacement or its time derivatives (Clough and Penzien, 1993). $\theta\ (t)$ is the flap angle of rotation, and $\dot{\theta}$, $\ddot{\theta}$ are its first and second-time derivatives.

The first two terms in the left-hand side of Equation (1) represent the moment of inertia and hydrostatic stiffness proportional to acceleration and displacement. Hydrostatic stiffness represents how the buoyancy and weight act on the body when it moves under wave actions. Change in centre of gravity, buoyancy, or the submerged volume affect the hydrostatic stiffness and make it change in time. In this study, it was assumed that both moments of inertia and hydrostatic stiffness are constant and are calculated analytically (Mei et al., 2005).

To represent the PTO effects, two parameters of PTO damping (C_P) and stiffness (K_P) are introduced (Marco, 2017). The procedure for defining the control framework and estimating the optimized values of K_P and C_P is described in Section 4.1.

The radiation damping is introduced by boundary condition on the flap surface, structural damping force caused by the hinge connections, and quadratic damping is also added to increase the accuracy of the model. Both quadratic and structural damping due to the hinge cannot be analytically calculated (Adhikari, 2000) and are extracted from the experimental tests. Structural damping coefficient (C_F) is extracted from experimental dry tests, and the quadratic coefficient (C_{QD}) is estimated from a hybrid physical and numerical simulation (Saeidtehrani, 2015).

During the experimental tests, it was found that it is not possible to find a unique value for the quadratic damping coefficient. This is aligned with previous studies indicating the difficulty in finding a unique value valid for the whole decay time-series response due to the high dependency of the drag term to the (K_c) or Reynolds number (Faltinsen, 1990). It was also found that the quadratic damping is highly amplitude-dependent as was reported for similar damping terms (Clough and Penzien, 1993). Therefore, two conditional terms in the equation are defined for the quadratic damping coefficient: C_{QD1} for rotation equal and more than 1 radian, and C_{QD2} for rotation less than 1 radian which is almost equal to the angle that flap is completely submerged in the water.

It should be emphasized that by increasing the amplitude of the oscillation, nonlinear wave-structure effects are increased and the presence of quadratic damping in the equation, as a nonlinear term, assures the capturing of the nonlinear expected behaviour (Alenitsyn et al., 1997; Butikov, 1999; Nayfeh and Mook, 1979).

The right-hand side of Equation (1) is simulating the dynamic pressure on the flap surface. h_r and w indicates the coordinate of the centre of rotation and the width of the flap. In this equation:

ρ is the density of water;
ϕ_t is the time derivative of the fluid flow velocity potential;
n is the unit normal vector pointing into the body.

It should be noted that the right-hand side integration domain is on

the submerged floating body at rest position. By substituting p (dynamic pressure) with the derivative of potential linearized first order Bernoulli (E. Renzi, A. Abdolali and Dias, 2012), this mathematical description can connect the equation of flap's motion to the potential flow describing the velocity field around the flap which is obtained from the solution of the Laplace equation:

$$\nabla^2\phi = 0 \tag{2}$$

By solving the Laplace equation in a domain with appropriate boundary conditions which define how flow behaves at a certain boundary (Svendsen, 2006); the radiation, diffraction, and incident potential problems are solved simultaneously.

The impermeable bottom surface ($atz = -d$) is described by zero flux condition$\phi_z = 0$. The free surface boundary condition is obtained by combining the kinematic and dynamic conditions which can be implemented as linear (C.-H. Lee, 1995), however, in this project, it is simulated as:

$$\phi_{tt} + g\phi_z = 0 \quad at\ z = 0 \tag{3}$$

By introducing a boundary condition bonding the flap motion to the fluid, the diffraction is simulated in combination with radiation, it is explained by using the decomposition of the total potential as a sum of the incident, diffraction, and radiation potentials($\phi = \phi_I + \phi_D + \phi_R$), in which $\phi_R = \sum_{\alpha} V_\alpha \phi_\alpha$ describes the radiation potential for 6 degrees of freedom ($\alpha = 1,2, \ldots,6$). ϕ_I and ϕ_D are incident and diffraction potential, respectively. V_α is the generalized body velocity. It is known that the derivative of the sum of the incident and diffraction potential normal to the body surface is zero and the derivative of radiation potential normal to the body surface is n_α, the generalized normal vector. Therefore, the derivative of total potentials normal to the body surface would be $\phi_n = \sum_{\alpha} V_\alpha n_\alpha$ (Mei, 2012). The boundary condition on the flap surface is defined as:

$$\phi_n = \frac{\partial\theta}{\partial t}(z - h_r) \tag{4}$$

Hence, the fluid velocity is directly connected to flap motion via linking flap's velocity to fluid velocity and also connecting an Ordinary Differential Equation (ODE) describing flap's motion to Partial Differential Equation (PDE) representing the fluid flow rather than frequency-dependent parameters (i.e. added mass and damping) that may be more effective near to the natural frequency (Jia, 2014).

The surrounding walls are simulated by using the reflective boundary conditions$\nabla\phi = 0$, and a wave-maker boundary condition for both generating and absorbing waves is mathematically defined as (Flick and Guza, 1980; Kusumawinahyu et al., 2017):

$$\phi_x = \frac{-k}{\omega}\phi_t + \frac{g \times H \times k \times cosh(k \times (d+z))}{\omega \times cosh(k \times d)} cos(\omega t - kx) \tag{5}$$

ω and g are wave angular frequency and the gravity acceleration, respectively.

A summary of the boundary conditions and a schematic view of the mathematical formulation. is presented in Fig. 4.

3.3. Numerical model verification by experimental tests

This part addresses the verification of the developed numerical model with experimental tests conducted in the wave flume of the laboratory of Roma Tre University. Three sets of experimental studies and the corresponding numerical simulations have been conducted to study the 1:40 scale model in free oscillation dry tests, decay oscillation in water, and under regular wave actions (Saeidtehrani, 2015). During the experiments, the movements of flaps were recorded by a camera, and video-processing codes were developed to extract the time-series response of the flaps by Matlab ("Matlab," 2019).

The first set of experiments, free oscillation time-series, have been conducted to extract the friction of the hinge by putting the device upside down in a way that the flaps acted like a pendulum. Then the device was set in the flume for performing tests in water. Fig. 5 shows the as-built dimensions for the experimental simulation. The flaps had a dimension of 72.5 *mm* (*height*) *x* 50 *mm* (*width*) *x* 45 *mm* (*length*) with $1 \sim 2$ *mm* tolerance. As previously mentioned, the water depth in the flume was set equal to 300 mm and 50 *mm* of the flap height (72.5*mm*) was underwater.

The second set of experiments, decay oscillation in water, have been used in combination with numerical simulation to extract the quadratic damping coefficient and the damped natural period. The extracted damping coefficients from the experimental tests are used as an approximation for the loss of energy which cannot be mathematically calculated due to the complexities of the mathematical formulation for physical damping (Adhikari, 2000).

For the third set of experiments, response to wave action, regular waves with 50 *mm* wave height, and a period in the range of 0.3 to 1.1 s were considered which not only covers the maximum expected wave period but also covers the wave periods corresponding to the damped natural period of the flaps estimated from the decay oscillation in water (Saeidtehrani, 2015). It was shown that the natural periods of the flaps are different because of the flap's location, their boundary condition

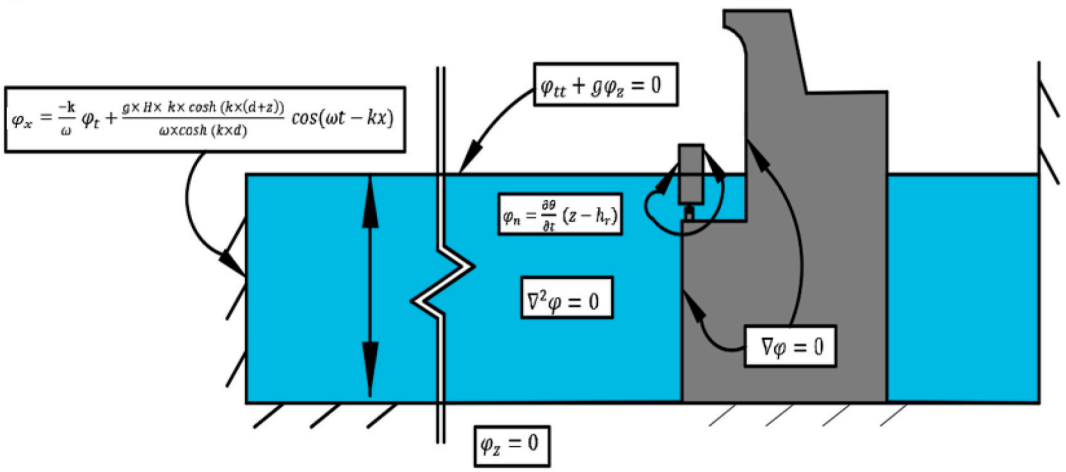

Fig. 4. Schematic of mathematical formulation.

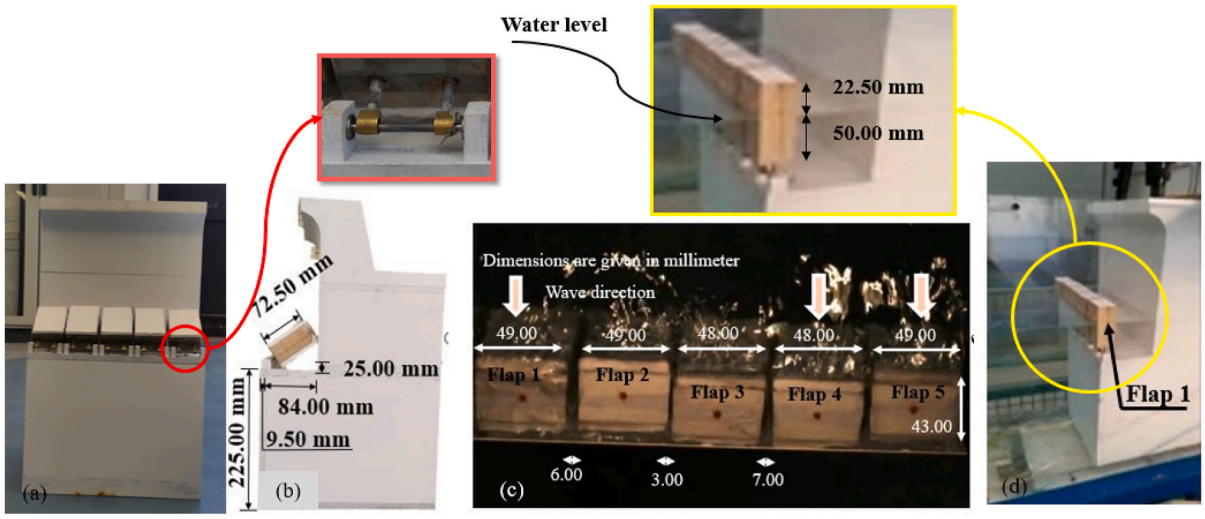

Fig. 5. Experimental tests: a) Frontal view, b) Side view, c) Top view, and d) Set up in the flume.

(proximity of two flaps to the lateral flume's walls), and the inherent differences due to the construction. Construction effects incorporate different dimensions and gaps between flaps (see Fig. 5- c), or diversity of the friction of hinges and their effects on the damped natural period (Saeidtehrani, 2015).

As expected, by increasing the wave period and its corresponding wave force, the responses of all flaps are increasing; however, some differences in response to various wave periods were observed mainly due to the dissimilarity of the damped natural periods of the flaps.

The proximity of the wave period to each flap's damped natural period makes resonance for the specific flap which has the same damped natural period. Therefore, some out of phase responses can be observed in response to waves with period $[0.3, 05]s$. By increasing the wave periods more than the flap's damped natural period, the excitation of all flaps will be more or less the same, therefore they will oscillate in phase. Fig. 6 shows sample frames of experimental tests and the time-series responses, the out of phase response to wave period 0.4 s and in phase response to wave period 0.60 s can be observed in this figure.

Fig. 7 shows the comparison between the Root Mean Square (RMS) of the flaps amplitude extracted from the experimental simulation time-series with 3-D numerical simulation results over wave period in the range of0.3 to 1.1 s. Due to the nonlinearity of the flap's response (Saeidtehrani, 2015; Sammarco et al., 1997), RMS over other linear parameters such as Response Amplitude Operation (RAO) (Chakrabarti, 1987; Karimirad, 2014b) is chosen.

For better comparison and the sake of clarity, only the numerical response of the middle flap, Flap 3, is presented versus the experimental results of all five flaps. This comparison has the benefit to provide an idea that how much the response of an individual flap is different from a middle flap which can be considered as the representative middle flap in an array.

Some local peaks due to the nonlinear resonance (Alenitsyn et al., 1997; Butikov, 1999; Nayfeh and Mook, 1979) in response to waves with periods equal to 0.68, 0.70, 0.90, and 1.00 s are seen in Fig. 7. When two flaps experience the resonant, all flaps undergo maximum response due to the simultaneous change in the surrounding hydrodynamic by two flaps. However, in case that only one flap resonates with the incoming wave, the local peak for all flaps doesn't happen, this is observed in the response to wave period 1.00 s.

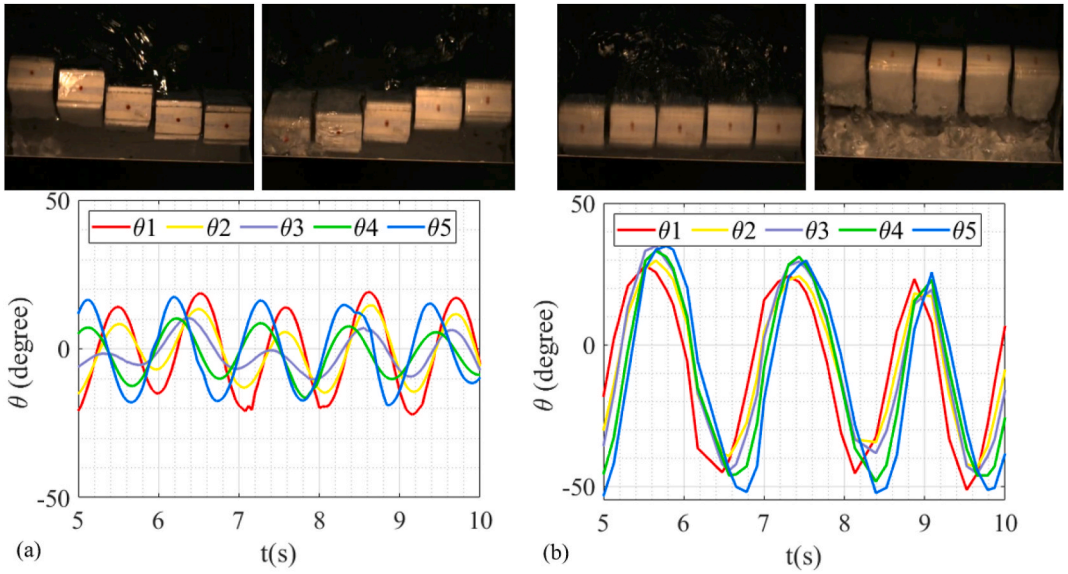

Fig. 6. Sample frames of experimental tests and the time-series responses: a) out of phase movements of flaps in response to wave period 0.40*s*, b) in phase movements of flaps in response to wave period 0.60 *s*.

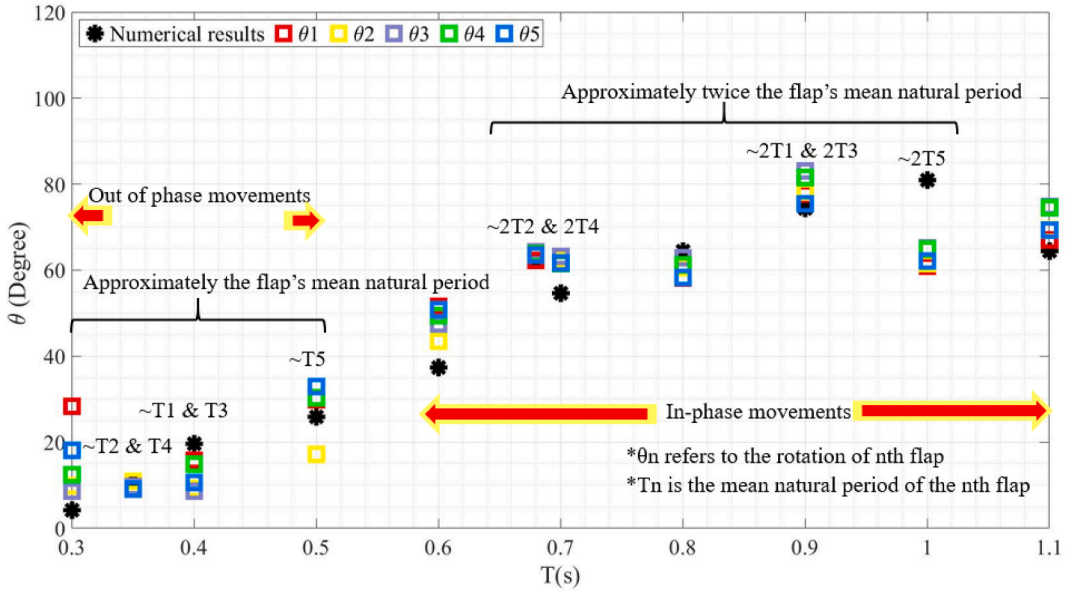

Fig. 7. Comparison of numerical and experimental seaward RMS responses of the flaps to wave action.

Fig. 7 shows that the numerical model was successful to simulate the experimental tests considering the involved nonlinearities. As previously mentioned, the numerical model has a nonlinear term that captures the nonlinear behaviour in wave-structure interaction (Saeidtehrani, 2015; Sammarco et al., 1997).

These nonlinearities are mainly due to the generation of waves by flaps, the presence of transverse waves, and the loss of energy because of vortex shedding and flow separation. Some of these phenomena are demonstrated by some frames from the experimental tests in Fig. 8.

The experimentally validated numerical tool is used for simulation of flap-type WEC with similar dimensions to what was studied in (Saeidtehrani, 2015) except adding 25 mm to the flap height to capture the whole power of the wave.

Therefore, a flap with dimensions $75mm(height)x50mm(width)x45mm(length)$ is used for the analyses. The corresponding moment of inertia and hydrostatic stiffness is analytically estimated (Mei et al., 2005) as $9.86 \times 10 - 5$ [kgm^2] and 0.028 [kgm^2 s^{-2}], respectively. From classic dynamic literature, the natural period would be 0.37 s which is almost half of the mean incoming wave period. The flaps are placed at a distance equal to $85mm$ (around 13% of flap height) to prevent the strike of flap to the breakwater when it becomes parallel to the horizon.

3.4. Sensitivity analyses of effective parameters

The sensitivity analyses have been carried out to obtain the required accuracy within the incurring computational time and cost. For each set of analyses, a base model with the effective parameters is selected and the variance of the parameters and the consequent changes in the numerical results such as the time-domain response of flap is assessed.

The first set of analyses is conducted to find the required domain length for the fairly accurate simulation. Then the required time step and mesh size for the simulation are studied. For each parameter, several simulations are conducted and the results are compared.

Fig. 9 shows the rotation time-series of the flap in domains with different lengths and flap distances from the wavemaker (FL). As can be seen in Fig. 9, the main response characteristics including the amplitude and the period are not affected by the flume length.

The only observed discrepancy is the phase difference of time-series responses due to the various required time for the wave to reach the flap (t_I) which are calculated and presented in the graph. All waves generated from distance $[1,\ 3]$ m reach the flap and make it oscillate with the maximum amplitude after 5 s, and then all time-series responses have almost the same amplitude and frequency. Therefore, the RMS of the response in time duration $[5, 10]s$ is calculated and presented in Fig. 9; as can be seen, the maximum difference between θ_{RMS} values are almost less than 1.8 %.

According to the results and for the sake of computational cost, the length equal to 1 m is selected for further analyses. The next step is to demonstrate the mathematical and logical reasons for selecting the mesh size and the time step.

The accuracy and stability of a numerical method for structural dynamic analyses are compared and related to the ratio of time step to the shortest natural period of the system (Gavin, 2016). For such a multidisciplinary project, the time step is selected considering the minimum

Fig. 8. a) Presence of transverse waves, b) Flow separation and turbulence, c) Vortex shedding.

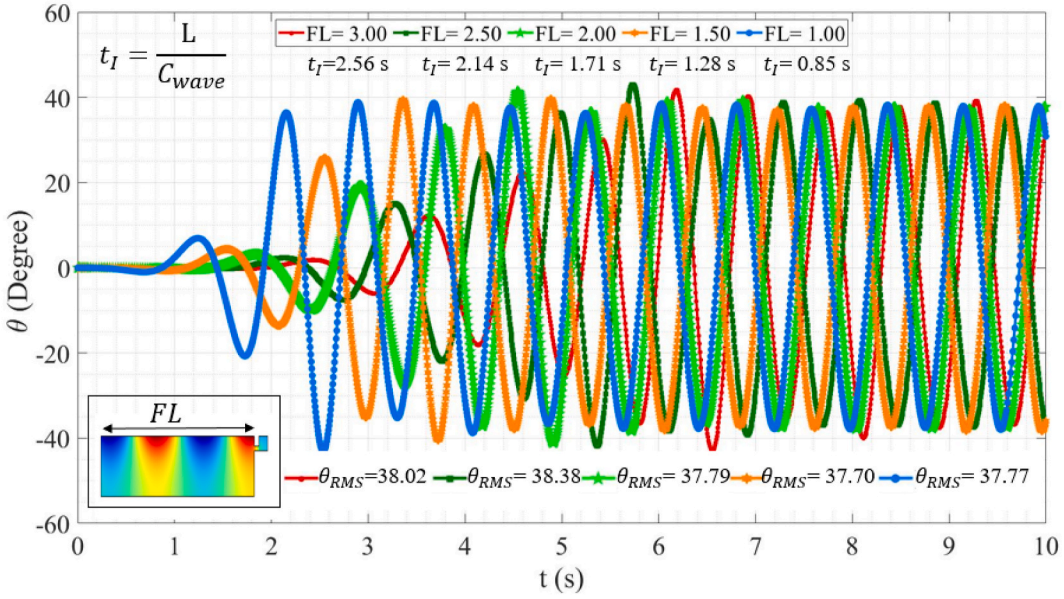

Fig. 9. Flap rotation time-series considering different domain lengths.

of the incoming wave period and the natural period.

Although the small time step could lead to more accurate numerical results (Jia, 2014) for capturing the nonlinear behaviour (Clough and Penzien, 1993); it increases the computational time and efforts for both analyses and data post-processing. Therefore, it is crucial to find a proper and efficient time step for dynamic analyses which is generally equal to one-tenth to one-fifth of the minimum natural period, and the exciting force (Humar and Carleton, 2012).

Proper maximum element size and the time step can be estimated by Courant number ($u\Delta t/\Delta x$) that is also referred to as the Courant-Friedrichs-Lewy or CFL condition, where u is the velocity, Δt, and Δx are the time step and the length interval (Anderson et al., 2016).

For this study, velocity will be the celerity of the wave which can be an incoming wave, a wave generated by the flap, or radiated waves from the breakwater. The courant number less than 1 is suggested for the wave equation (Anderson et al., 2016), this value should be decreased to a range between 0.90 and 0.95 for dynamic analyses (Jia, 2014). The analyses were repeated with different time steps and element sizes and the ratio was compared with the above-recommended values; consequently, practical and efficient time step and mesh size have been chosen for further studies.

Fig. 10 shows a maximum 1.2 % difference between the θ_{max} for fine and normal mesh, and less than 0.1% difference for other response parameters. Therefore, for the sake of computational saving, fine mesh is

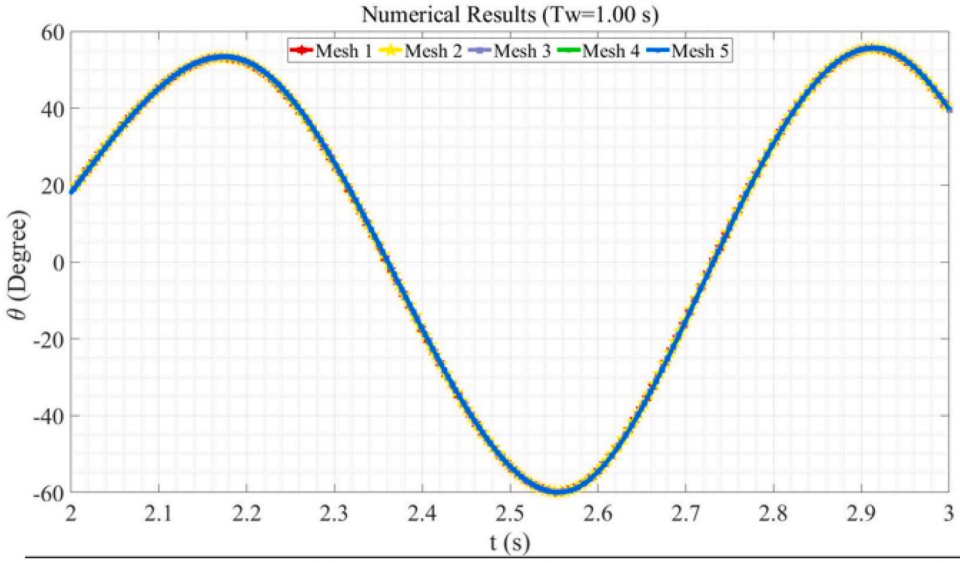

Mesh	Maximum ES (m)	Minimum ES (m)	θ_{mean}	θ_{max}	T_{mean}	T_s
Normal	0.0135	6.0E-4	47.24	56.53	0.84	0.78
Fine	0.0105	3.0E-4	47.34	56.64	0.84	0.79
Finer	0.0084	1.2E-4	47.39	56.69	0.85	0.79
Extra fine	0.0039	4.5E-5	47.41	56.71	0.85	0.79

Fig. 10. Mesh sensitivity analyses and response characteristics.

chosen for analyses.

An efficient time-stepping procedure with $\Delta t = 0.01\,s$ and the tolerance of 0.001 *s*to control the internal time steps is chosen for the studies which provide the same accuracy with $\Delta t = 0.001\,s$. Fig. 11 demonstrates the wave propagation when the wave reaches the flap from breakwater or wavemaker. As can be seen, the particle path is completely reminding the fluid particle path in intermediate water depth (Holthuijsen, 2010) which was also theoretically predicted (see 3.1). By estimating compelling values of FL,Δt, and Δx for the numerical simulation, the analyses can be conducted for the investigation of design properties.

4. Investigation of design properties

This section is dedicated to providing a thorough understanding of the effects of design properties such as the flap's distance from the breakwater and PTO coefficients on the amplitude of oscillation and the power absorbance. The first part presents the control framework and the optimization of PTO coefficients. Later the device is studied to find an optimized place for mounting the flaps on the breakwater.

The optimization Nelder Mendeley algorithm is used for this study; this derivative-free algorithm benefits from quick convergence and is based on the three possible scenarios as worse, good, and best. The procedure is repetitive to eliminate the worse condition in each step (Audet and Hare, 2018). The primary optimization analyses are conducted by using a 2-D simulation; however, the results are further controlled with a 3-D model.

4.1. Control system framework and calculation of PTO coefficients

The diversity of WEC concepts cause a variety of PTOs (Ahamed et al., 2020), but some recognized types are more suitable for oscillating wave energy converters (Marco, 2017; Têtu, 2017). Apart from the variety of PTOs, the goal here is to develop a more accurate numerical simulation for representing the expected behaviour of the proposed device considering the PTO damping and stiffness.

PTO damping is directly related to power extraction (Rodríguez et al., 2019) and its rise could increase the power to some extend (Nolte and Ertekin, 2014). The power absorbance can be estimated by $\frac{1}{T_w}\int_0^{T_w} C_P\dot{\theta}^2 dt$ for flap rotation over a wave period (E. Renzi, A. Abdolali and Dias, 2012; Folley, 2016). While the average wave power per unit wave-front length ($\mathrm{kg.m/s^3 = watt/}m$) can be expressed as (Algieri Ferraro et al., 2017):

$$P_w = \frac{\rho g^2}{64\pi}\left(H^2T\right)\left[1+\frac{2Kd}{sinh2Kd}\right]tanhKd \tag{6}$$

P_w is the average wave power per unit wave-front length, therefore should be multiplied by the width of all the WEC components involved in energy conversion to be comparable with the power absorbance (Pecher, 2017).

Some studies suggested that the maximum power can be captured when C_P is equal to the hydrodynamic damping coefficient (Folley, 2016) or radiation damping for the theoretical estimation of power absorbance (Paolo Sammarco et al., 2016).

The PTO stiffness coefficient can be consequently tunned to make resonance in the system (Saeidtehrani et al., 2017). Section 6-Appendix A explains the possible theoretical correlation between PTO damping and stiffness for maximizing the energy extraction; however, for this study, the numerical simulation representing the flap-type WEC is combined with the optimization algorithm to find the optimized values of PTO coefficients. The upper bound of the PTO damping is selected to make the system oscillate under-critically (see Fig. 17, Section 6-Appendix A).

Oscillation time-series responses and the corresponding power, and Capture Width Ratio ($CWR = P_{abs}/(width_{active} * P_w)$) for some of the PTO sets are presented in Fig. 12. CWR is a non-dimensional performance ratio of the absorbed power (watt) to the available power ($\mathrm{watt/}m$) multiplied by the active width (m) that is the width of all the device components involved in the energy conversion from waves to absorbed energy (Pecher, 2017), for flap-type WEC, active width is the width of the flap. *CWR* represents the effectiveness of the WEC device to absorb the wave energy (Pecher and Kofoed, 2017); this ratio is also called hydrodynamic performance in some literature (Babarit, 2015).

The maximum oscillation amplitude at time 2.5 s is also zoomed in Fig. 12 which highlights the influence of different PTO coefficients on the response amplitude. The maximum CWR is obtained for PTO damping and stiffness equal to 3.80×10^{-3} (kgm^2/s) and 4.00×10^{-4} (kgm^2/s^2) which is shown by marking a green outline around the PTO properties.

According to the formula of power absorbance, power is dependent

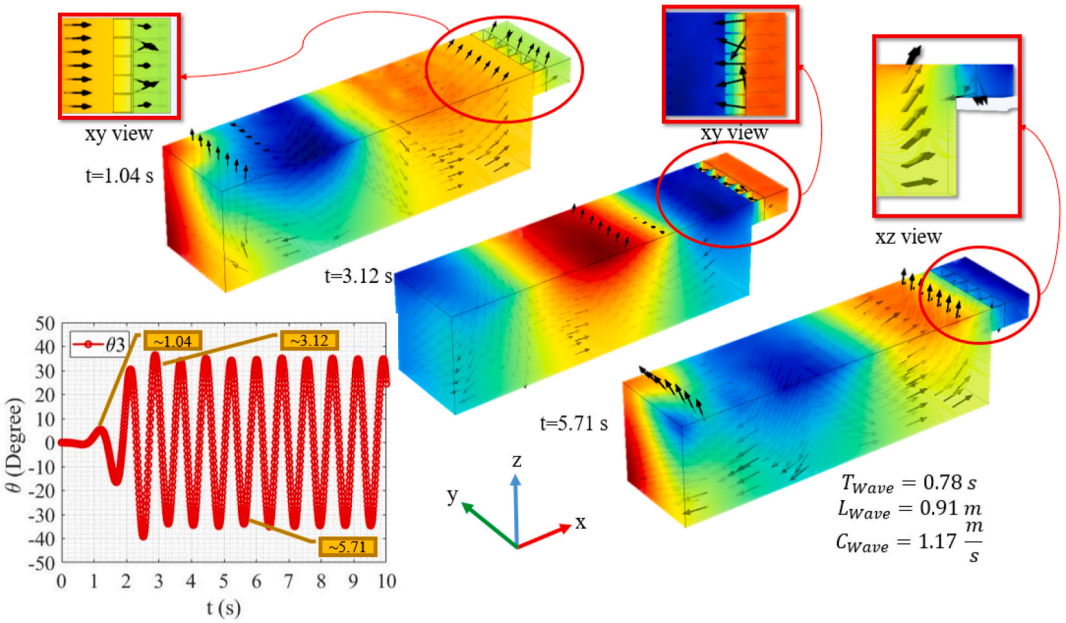

Fig. 11. 3-D simulation of five flaps standing on the breakwater.

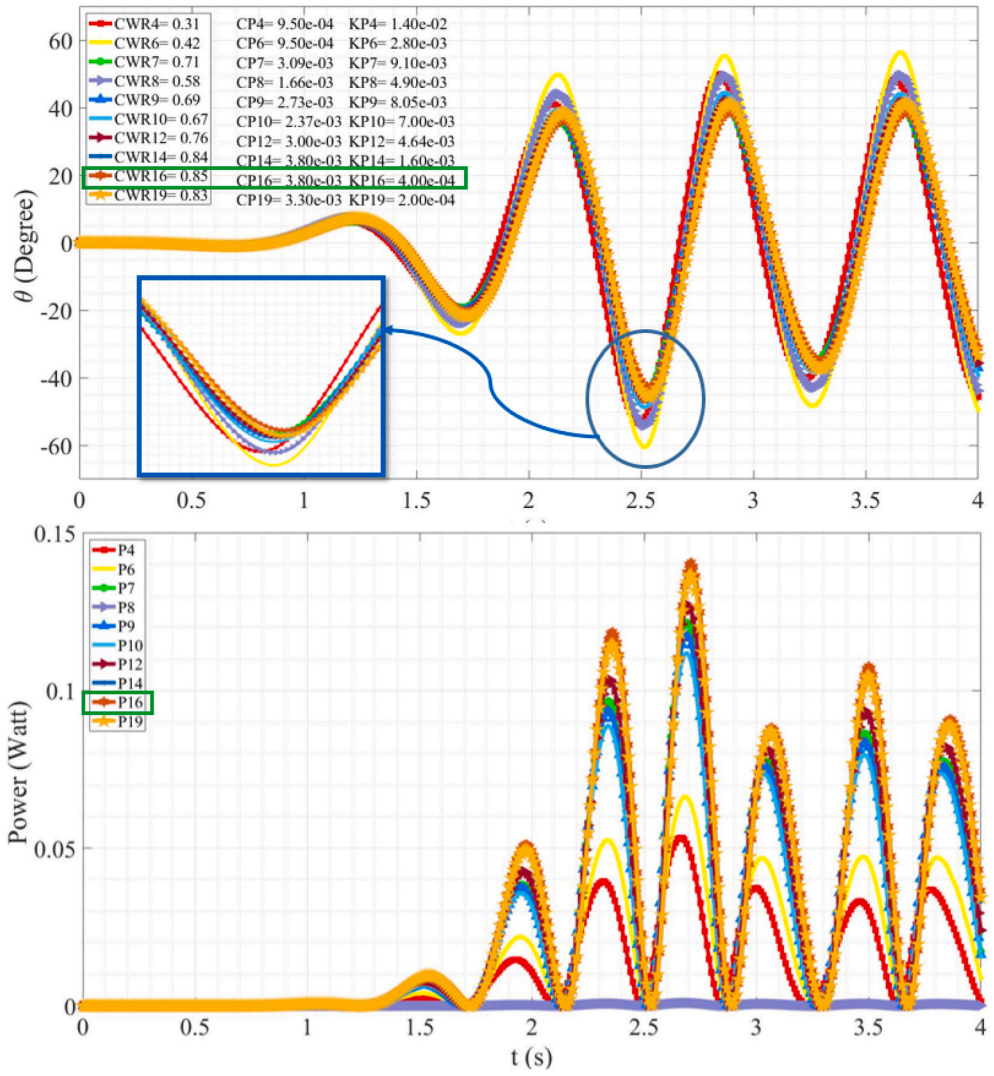

Fig. 12. Time-series oscillation and extracted power for various PTO coefficients.

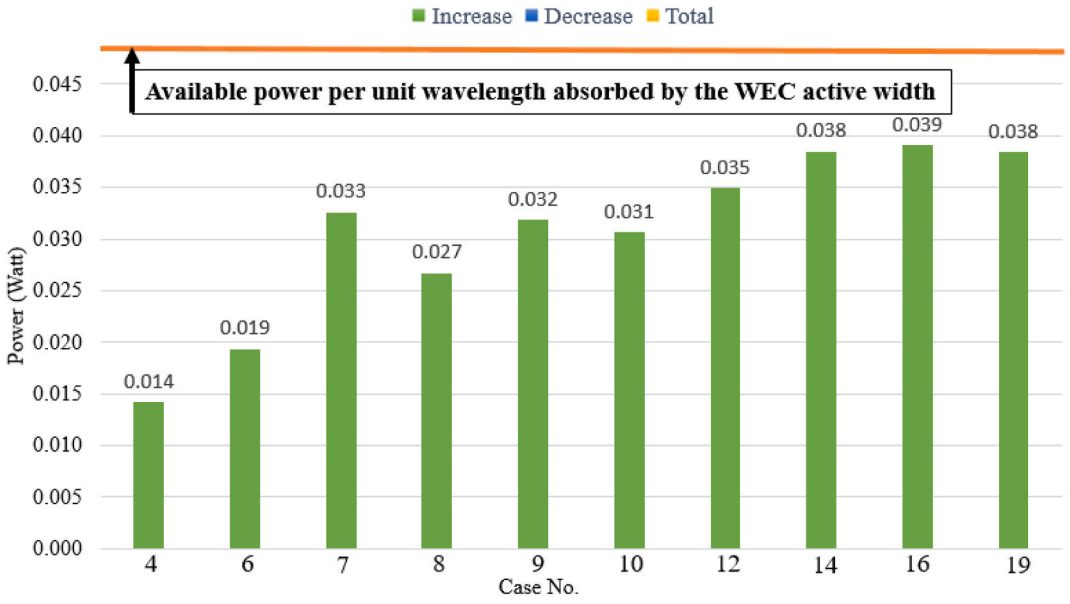

Fig. 13. Extracted power for various PTO coefficients over a wave period.

on two variables, velocity, and PTO damping. Flap's motion and velocity have 90-degree phase differences, which cause that maximum of power happens when the oscillation is zero, this time-lag can be observed in Fig. 12. Mathematically speaking, motion and velocity (the first time-derivative of motion) can be described by *sin* and *cos*term, respectively.

While the increase of PTO damping can enhance the power, its rise also decreases the amplitude of oscillation and velocity. From Fig. 12, it can be seen that for a smaller amount of PTO, the amplitude is increased but is not corresponding with the power enhancement.

As illustrated in Fig. 12, although there are some differences in extracted power over each wave cycle, the obtained PTO set 16provides the maximum power in the whole time-series. The comparison between the extracted power over one wave with the maximum available power absorbed by the WEC active width for wave period 0.78 s is shown in Fig. 13.

The responses of flaps are prone to the presence of the breakwater, the PTO coefficients to calculate the power are obtained and optimized for a primary distance of flaps from the breakwater through Section 4.1. The next section is dedicated to theoretically and numerically study the flaps and breakwater interaction and find a suitable location for the flap installation, later the parametric study and distance optimization is carried out to verify the proposed place.

4.2. Distance of the flap-type WECs from the breakwater

As was previously mentioned, the primary distance of the flaps from the breakwater is considered 85mm to prevent the strike of the flap to the breakwater when its rotation reaches or passes 90 degrees. The place of mounting flaps has consequences on the formation of waves behind the flaps and in a distance between the flaps and the breakwater. The presence of the incoming waves, the waves generated by the flaps, and the reflected waves from the wall form standing or group waves. The important feature of standing waves is stationary fluctuations with antinode and nodes which are the occurrence place of maximum and minimum amplitude.

The equations representing the waves in the domain and their corresponding period are presented in Section 7 -Appendix B. The theoretical description provided in this section suggests that $\omega_d, \overline{\omega}$are the dominant wave frequencies in the first cycles of the response, with the standing wave frequency equal to $(\omega_d + \overline{\omega})/2$ (see Section 7- Appendix B).

The modal activity of the confined water between the flap and the breakwater occurs at frequencies corresponding to the confined water dimensions. The first axial mode is activated when the distance is equal to half of the wave that disturbs the domain. The presence of different waves and their effects on the response is illustrated in Fig. 14 which shows the parametric study on flap's distance from the reflection wall.

Some of the specific distances cause a major difference in the flap's response amplitude, so it is important to figure out what is the reason behind it and how they could affect the response. By using the study outcomes, it would be possible to tune the distance to increase the amplitude of oscillation and the power.

For example, the distance equal to 0.60 m, which is shown with a black line in Fig. 14, is almost equal to half of the wavelength corresponding to the $(\omega_d + \overline{\omega})/2$. It can be seen that its direct effect is increasing the response, however, this effect is diminished after around 6 s, when the transient response is damped out. Therefore, after a while and by increasing the dominancy effect of steady response, the minimum amplitude is observed for $= 0.60\ m$.

The maximum amplitudes in the first cycles, red and yellow lines with corresponding distances equal to 0.08 *m* and 0.12 *m* happened near the wavelength of the flap's natural frequency (0.11 m). It should be emphasized that mathematical representation of resonance is the denominator of the steady response term, however, after a while, due to the presence of a different source of damping it decreased (Clough and Penzien, 1993). Comparing the maximum flap response amplitude between $d = 0.08$ and $d = 0.60$. *m* shows an almost 28% difference in the first cycles, and 87% in the next cycles in the time series response, which reflects the importance of finding a proper place for mounting the flap.

It is anticipated that due to the dominancy of the incoming wave frequency after vanishing the transient response, the other maximum happened at distance equal to the half of wavelength (~ 0.44 m) corresponding to the incoming wave period. Although, at this distance, the response is higher in comparison to 0.48 m; the maximum is observed in the distance equal to 0.36 m which approximately corresponds to a half wavelength of two times the flap's natural period.

It should be noted that the relation between different frequencies and the value of damping could significantly change the governing frequency of the wave in the domain. Based on the above-mentioned findings; if the wave resource has the short-variability, the location of antinode based on the natural frequency of the flap is justified; however, in case that long span variability in wave characteristics is expected, it

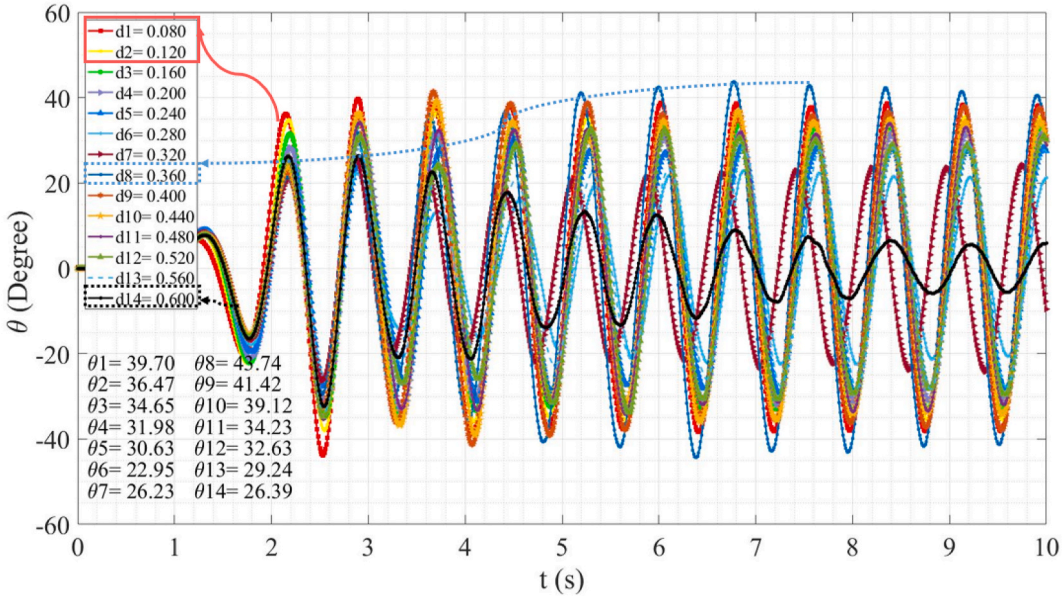

Fig. 14. Parametric study of flap's distance from the breakwater.

would be logical to consider other frequencies such as wave frequency and the possible sub or super-harmonic resonance which can increase the motion amplitude and consequently the waves generated by flaps in the domain.

From Fig. 14, it can be seen that mounting flap at distance equal to $\sim 0.08$and $0.36m$ can make the maximum oscillation in the response time-series. When the transient response is dominant, placement of flap at distance equal to $\sim 0.08m$ make the maximum response; while for the steady response, the maximum happens when the flap stands at a distance equal to $0.36m$. However, the maximum amplitude difference when the flap is mounted at $0.08$and $0.36m$ is less than 12% in the whole time-series response. Therefore, it is possible to limit our optimization time and find the optimized value that makes the maximum response in the first few response cycles.

Fig. 15 shows the results of another set of numerical simulations in combination with an optimization algorithm to control the power extraction corresponding to the change in the flap's distance from the reflection wall. For this set of analyses, the obtained optimized PTO coefficients from Section 4.1 have been used. The vertical wall coordinate is considered a control variable, and the objective function is power. The maximum distance was set equal to 350 mm considering the maximum distance equal to 14.00 m from the vertical wall in the real situation.

The maximum response at time 2.5 s to highlight the amplitude difference caused by various distances from the vertical wall is zoomed in Fig. 15. The calculated *CWRs* show that the maximum power (marked and highlighted with red and purple line) is obtained at distance equal to 0.085, and 0.109 which are the nearest ones to the place of the antinode of the natural frequency. It must be stressed that the minimum *CWR* is near to $1/6$ of the maximum *CWR* which proves the importance of the optimized placement of flaps on the breakwater.

As already stated in Section 3.3, it is expected that the flaps tend to move together in response to wave periods $[0.6, 1]s$; this tendency causes that the 2-D model to effectively represent the device behaviour. However, to numerically demonstrate the efficiency of the 2-D model, the next section is dedicated to studying the device behaviour by using a 3-D simulation model of the flaps with the same mass properties and dimensions as proposed for the 2-D simulation.

4.3. 3-D simulation considering the proposed distance and the optimized PTO coefficients

This section presents the numerical results of a 3-D simulation of the five flaps mounted on the breakwater with the optimized PTO coefficients and the distance from the reflective wall obtained from the previous 2-D simulation (see *Sections* 4.1 *and* 4.2). The mathematical model is the same as Equation (1) which was explained in Section 3.2; however, for 3-D simulation, five Ordinary Differential Equations (ODEs) are defined for five flaps. By introducing the boundary condition on each flap surface and bonding the ODE equation to a Partial Differential Equation (PDE) representing flow velocity around the flap, the movement of each flap is connected with other flaps' rotation by the surrounding hydrodynamics.

For this study, it was assumed that all flaps share the same dynamic characteristics and only their location in an array can make some difference in their behaviour. This insignificant difference doesn't make a change in the flaps tendency to move together which was also observed in the experimental simulation for wave period $[0.61]s$; so, it is expected that the 2-D simulation effectively represents the flap's behaviour.

This subject is numerically investigated by a 3-D model incorporating the optimization PTO algorithm. For the sake of clarity and since the flaps move together and there is only an insignificant difference in their amplitude of oscillation, only the time-series response of the middle flap is presented in Fig. 16.

The similarity of the flaps' behaviour is also observed from the pie diagram which shows the *CWR* for each flap for optimized PTO set 26. As illustrated in the pie diagram, the *CWR* of the flaps has a maximum 10 % difference with each other, and as expected the flaps tend to move together (see Section 3.3) with a negligible difference in the maximum amplitude. The detailed information on the PTO sets, the extracted power over one wave, and the *CWRs* are also tabulated in Fig. 16, as was highlighted the maximum power can be captured by PTO set 26.

The optimized values for PTO and the distance from the breakwater were estimated by a 2-D simulation. The results have been controlled by a 3-D model, which shows that the maximum power can be achieved by the same PTO damping obtained from 2-D analyses, however, the PTO stiffness with a lower value produces more power. The estimated power

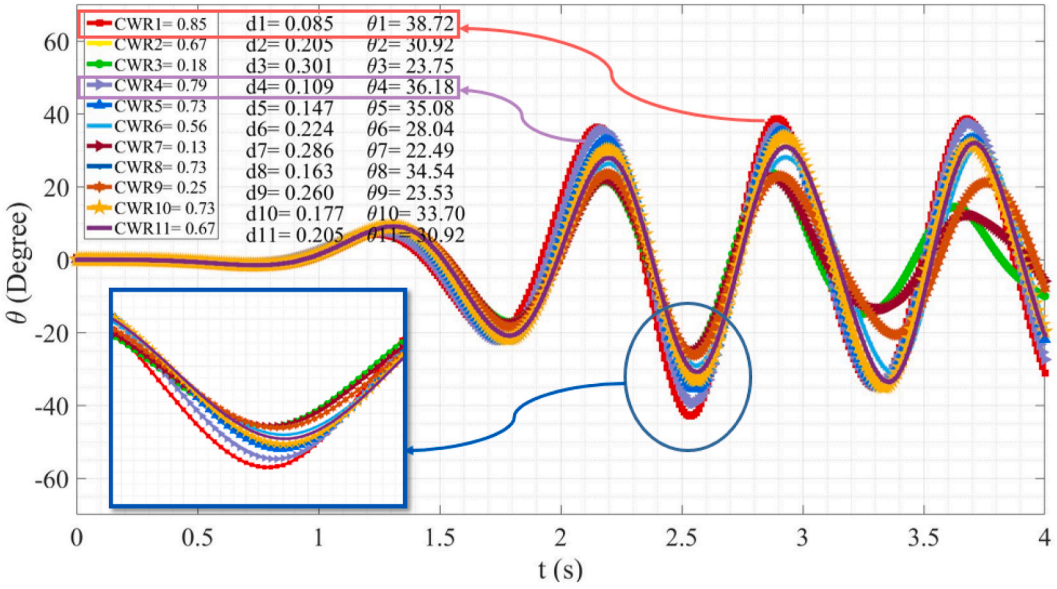

Fig. 15. Optimization of flap's distance from the breakwater.

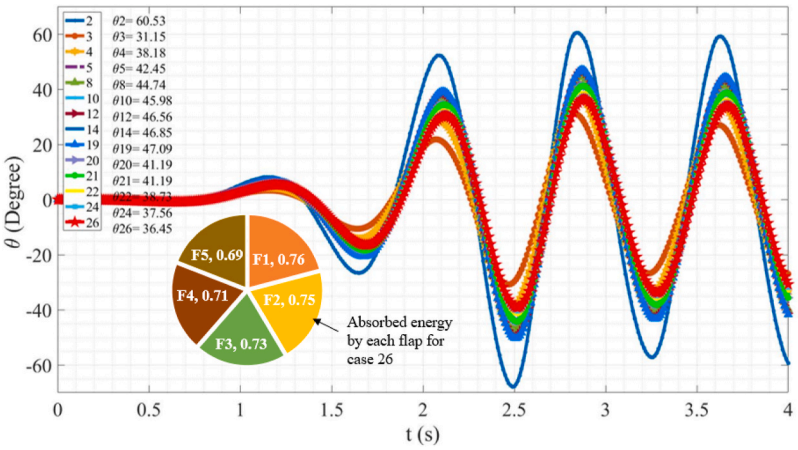

Case No.	CP (kg.m²/s)	KP(kg.m²/s²)	Power(Watt)	CWR
2	0.000E+00	0.000E+00	0.00	0.00
3	3.800E-03	2.800E-02	0.02	0.46
4	2.850E-03	1.400E-02	0.03	0.55
5	2.375E-03	7.000E-03	0.03	0.58
8	2.138E-03	3.500E-03	0.03	0.60
10	2.019E-03	1.750E-03	0.03	0.60
12	1.959E-03	8.750E-04	0.03	0.60
14	1.930E-03	4.375E-04	0.03	0.60
19	1.900E-03	0.000E+00	0.03	0.60
20	2.850E-03	0.000E+00	0.03	0.70
21	2.850E-03	0.000E+00	0.03	0.70
22	3.325E-03	0.000E+00	0.03	0.72
24	3.563E-03	0.000E+00	0.03	0.72
26	3.800E-03	2.375E-04	0.03	0.73

Fig. 16. Rotation time-series for various PTO sets and the corresponding power over a wave period.

from 2-D and 3-D simulations has less than a 14% difference which affirms that the 2-D simulation is successful in representing the flap's nonlinear dynamic behaviour and the corresponding power.

As it was mentioned in Section 2, the range of the high potential wave period is $[0.6, 1]$ *s*. It is shown in Appendix B, by tuning the flap characteristics with the average exciting wave period (0.78 *s*, see Fig. 1), the device represents a larger bandwidth due to the time-variability of dynamic characteristics and amplitude-dependency of damping. As it was explained and shown in Figs. 18 and 19, the expected range of damped natural period with the presence of PTO coefficients is $[0.60, 1.52]$ *s*. Presence of various damped natural period cause that the response to different exciting waves with the same range of period will be amplified due to different types of resonance (Butikov, 1999). This ensures the higher efficiency of the device in the real sea with various wave frequencies.

5. Conclusion

The goal of this research was to get a deep understanding of the nonlinear dynamic behaviour of flaps' array integrated into a breakwater by an experimentally verified numerical tool combined with the parametric and optimization procedure to increase the power absorbance.

It was shown that for the range of the high-energy potential wave periods, the flaps tend to oscillate together with an insignificant phase difference. As was demonstrated, the flap response to this range of wave period do not have significant motion difference, the flaps oscillate in phase, and therefore, the overall power from an array of flaps can be estimated by multiplying the number of flaps on average estimated power from 2D simulation. Hence, the 2-D model could effectively simulate the flap's behaviour and provides a fairly accurate response estimation and benchmark on the range of the PTO coefficients and the distance from the breakwater.

The power estimated from 2-D and 3-D has less than a 14% difference, and the same optimized PTO damping value was approximated from both analyses. This approach to finding the range of the wave characteristics that can be simulated by a 2-D model provides an advantage for reducing the computational cost.

It has been found that the formation of standing or group waves due to the presence of oscillating flaps, reflecting waves from the breakwater, and the incoming waves could make a maximum of 87 % difference in the amplitude of oscillation and decrease the efficiency of the device (measured by *CWR*) to 1/6. However, the proposed place for mounting the flaps based on the theoretical place of formation antinodes and considering the effects of confined water between the flap and the breakwater along with the optimized value of PTO coefficients leads to maximizing the power absorbance to 85 % of the available power.

It should be stressed that the design of an efficient device for all operational phases needs comprehensive study on different factors affecting the functionality of the WEC performance and finding the balance between different design goals such as maximum power extraction and survivability (Greaves and Iglesias, 2018). The goal of this paper was to maximize the power extraction and validate the concept which is considered as the first stages in the WEC development stages (Pecher and Costello, 2017). By tuning the device to increase the oscillation of flaps, the load on the body is increased and the consequences should be accurately investigated in future studies from various aspects such as durability of the material and connections that will affect the survivability of the device. This work could also be continued for developing the model to tunning the PTO system for random waves. In future studies, the interaction between the flaps will be effectively used to increase the frequency bandwidth and access a constant power absorbance for various dominant wave periods.

Declaration of competing interest

The authors declare that they have no known competing financial interests or personal relationships that could have appeared to influence the work reported in this paper.

Acknowledgment

This paper steps forward on the hydrodynamic analysis of flap-type WEC array integrated to a breakwater which was previously initiated during PhD studies of Saghy Saeidtehrani, and we would like to grab this opportunity to thank Professors Leopoldo Franco and Giorgio Bellotti for their support during PhD course at Roma Tre University.

6. Appendix A. Simplified control strategy

The resonance in an undamped system happens when the driving frequency is equal to the natural frequency of the system, but in a damped oscillation, the resonance frequency would be different. The natural period of the flap is $2\pi\sqrt{I/(K_P + K_H)}$ with considering the PTO stiffness effect; therefore, T_d would be equal to:

$$T_d^2 = \frac{T^2}{1 - \frac{(C_r + C_P)^2}{C_{Cr}^2}} \tag{A.1}$$

Considering the maximum energy capture with equality of PTO damping with radiation damping, C_r (Paolo Sammarco et al., 2016):

$$T_d^2 = \frac{T^2}{1 - \frac{4C_P^2}{C_{CR}^2}} \tag{A.2}$$

C_{Cr} is critical damping and is equal to $C_{Cr} = 2I\omega = \frac{4I\pi}{T}$, that leads to:

$$I(K_P + K_H) - C_P^2 = \frac{4\pi^2 I^2}{T_d^2} \tag{A.3}$$

$$K_P = \frac{4\pi^2 I}{T_d^2} + \frac{C_P^2}{I} - K_H \tag{A.4}$$

By having $I$and K_H, from the analytical formula (see (Mei et al., 2005)), this equation provides a relation between PTO damping and stiffness.

It is important to understand that the base of these equations and the similar formula is a linear assumption. Otherwise, the effect of damping or stiffness from different sources cannot be superposed, therefore it involves lots of uncertainties.

Theoretically, it is possible to have several sets of PTO coefficients to satisfy Equation (A.4); but the efficient set absorbs the maximum power while implementing the minimum damping and stiffness to the system. To find the optimized PTO coefficients, an optimization algorithm with the maximum power as an objective function is developed and combined with the time domain numerical simulation for flap oscillation under wave action.

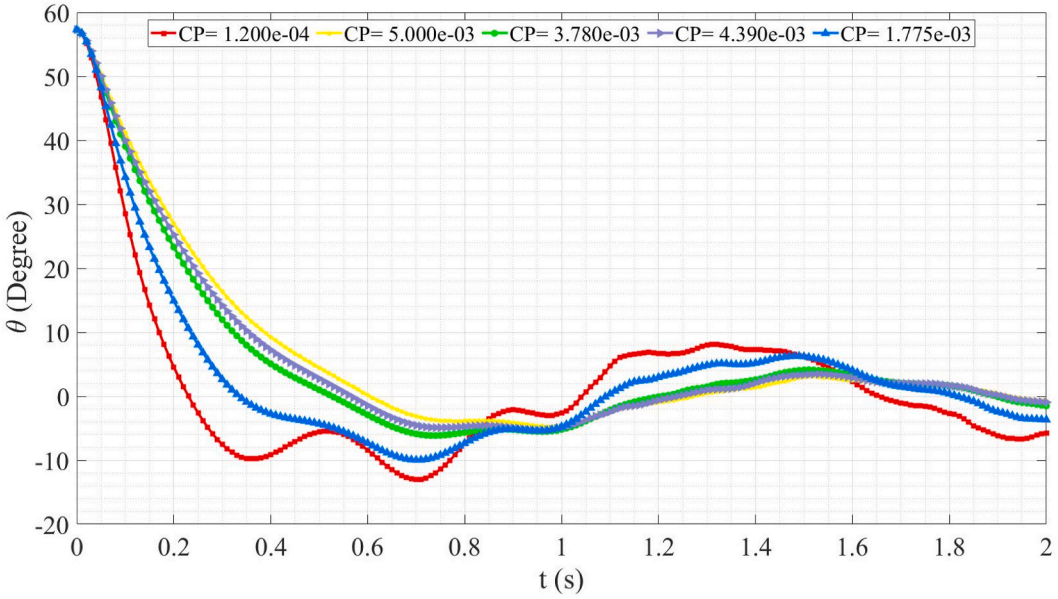

Fig. 17. Decay oscillation for finding maximum applicable C_P.

$C_{cr} - C_F$ is selected as the upper bound value for C_P to address a wide range of practical damping owing to the important contribution of higher PTO damping in enhancing the power. To explain the reason behind the selection of C_{cr}, it is convenient to describe three different motion types of critically, under-critically, and overcritically damped systems. C_{cr}draws a line between oscillatory and non-oscillatory systems (Jia, 2014). Under-critically systems are the only ones that oscillate around their equilibrium and are mostly described by the exponential decrease of the oscillation amplitude over time. Overcritically-damped has a slow movement to the equilibrium in comparison to the quickest approach of the critically damped systems toward the zero position.

C_{cr} can be estimated by the simplified harmonic formula, however, for an accurate approximation, decay oscillation analyses are combined with the optimization Nelder Mendeley algorithm to find the maximum under-critical damping. Other sources of damping such as friction of hinges and quadratic damping are introduced in the numerical simulation. From the results (see Fig. 17), the maximum $C_P = 3.8e - 3$ (kgm^2/s) is selected as the upper bound for under critically damped oscillation.

7. Appendix B. Standing wave equations and natural modes of the confined water

The confined water among the breakwater and flaps resembles the natural mode in a closed rectangular basin that is directly related to the basin geometry (Mei et al., 2005). Here the mode shape which is aligned with the direction of the wave train is the axial mode with $L = 2x$, in which x is the dimension of the confined water in the same direction. If the confined water is agitated, standing waves are formed with the frequency depending on the natural frequency of the basin and the frequency of the incoming wave.

Here, the incoming wave hits the flaps, and then the flaps start to oscillate, and the resultant wave train propagates in the confined water, and eventually reaches the wall, and reflected. As was previously mentioned and from basic wave theories, the interference of waves forms stationary wave

or wave groups in which the combination of just two sinusoidal waves with various amplitude and frequency leads to complicated solutions (Svendsen, 2006).

To study the present waves in the domain, and more specifically in the confined water, the dynamic response of an idealized mass-damper-spring system$m\ddot{v}+c\dot{v}+kv=P(t)$, with one degree of freedom under deterministic wave load, is considered, see (Clough and Penzien, 1993):

$$v(t)=(A\cos(\omega_d t)+B\sin(\omega_d t))e^{-\xi\omega t}+\frac{P_0}{K}\left(\frac{1}{(1-\beta^2)^2+(2\xi\beta)^2}\right)\left((1-\beta^2)\sin\overline{\omega}t-2\xi\beta\cos\overline{\omega}t\right) \tag{B.1}$$

At this point, it is more convenient to extend this equation based on only trigonometric functions:

$$A1=A \tag{B.2}$$

$$A2=B \tag{B.3}$$

$$A3=\frac{P_0}{K}\left(\frac{(1-\beta^2)}{(1-\beta^2)^2+(2\xi\beta)^2}\right) \tag{B.4}$$

$$A4=\frac{P_0}{K}\left(\frac{-2\xi\beta}{(1-\beta^2)^2+(2\xi\beta)^2}\right) \tag{B.5}$$

Thus:

$$v(t)=(A_1\cos(\omega_d t)+A_2\sin(\omega_D t))*e^{-\xi\omega t}+A_3\sin\overline{\omega}t+A_4\cos\overline{\omega}t) \tag{B.6}$$

This equation indicates that there are two dominant frequencies ω_d , $\overline{\omega}$ in the domain, in which the transient responses damped out after a while with $e^{-\xi\omega t}$ (Clough and Penzien, 1993). The presence of *cos* term make some phase delay in the response; however, it can be safely assumed that this equation is a combination of two *sin* terms with ω_d , $\overline{\omega}$ under the damping effect of $e^{-\xi\omega t}$. The denominator coefficients $A3$ and $A4$ can produce the dynamic amplification in the steady response which is generally called resonance (Clough and Penzien, 1993).

If the waves have the same frequency, the resulting linear super-harmonic wave has the following mathematical description (Svendsen, 2006):

$$y(x,t)=y_m\sin(kx-\omega t)+y_m\sin(kx+\omega t)=2y_m\cos(\omega t)\sin(kx) \tag{B.7}$$

However, if the existing waves have different frequencies, the resulting wave is described as (Svendsen, 2006):

$$y(x,t)=y_m\sin(k_a x-\omega_a t)+y_m\sin(k_b x+\omega_b t)=$$

$$2y_m\cos\left[\frac{k_a-k_b}{2}x-\frac{\omega_a-\omega_b}{2}t\right]\sin\left[\frac{k_a+k_b}{2}x-\frac{\omega_a+\omega_b}{2}t\right] \tag{B.8}$$

The generated wave train arrives at the wall, returned, and then is combined with the primary wave. Considering the complete reflection, it is expected that the combination of transient and stationary waves returning from the wall makes the additional frequencies such as $(\omega_d-\overline{\omega})/2$ and $(\omega_d+\overline{\omega})/2$. To have a clear illustration of the waves, the relation between the two frequency values should be clarified.

To calculate the ω_d, the decay analyses with the presence of PTO have been conducted, Fig. 18 shows the decay time-series responses with variable decay periods due to the presence of various sources of amplitude-dependent damping.

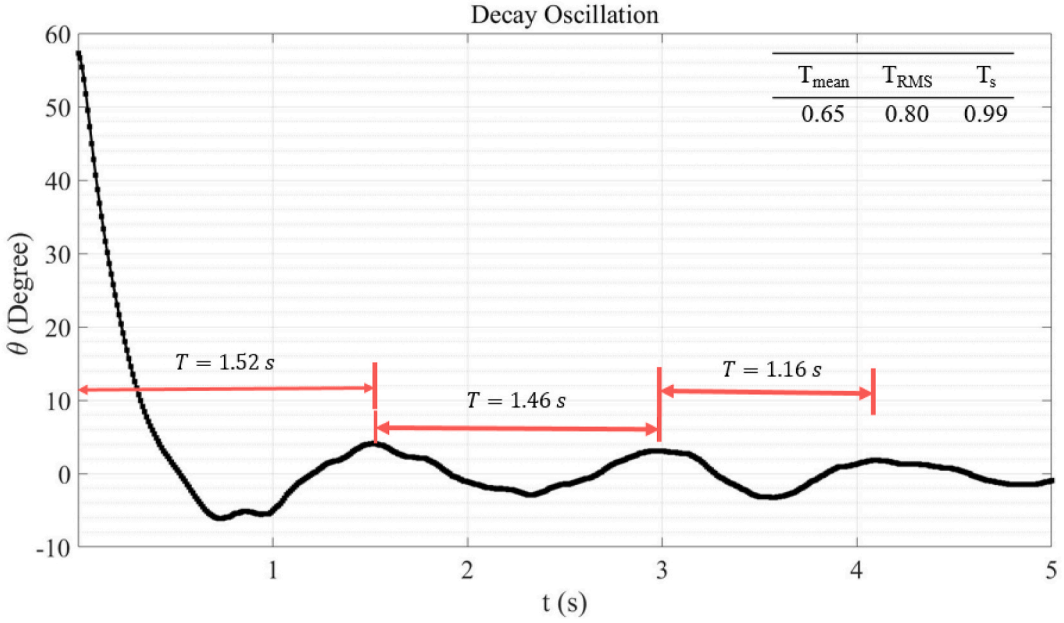

Fig. 18. Decay oscillation with presence of PTO coefficients.

According to the amplitude of oscillation around 40 degrees (see for example Fig. 12), it would be fair to assume that the damped period is around

1.46 s. The term with the higher frequency $(\omega_d + \overline{\omega})/2$varies much faster in comparison to other terms, so it is expected that the first cycles have the corresponding period of 1.00 s until the transient part is damped out. This subject is numerically studied by analyses of flap's response to wave period 0.78 s (see Fig. 19).

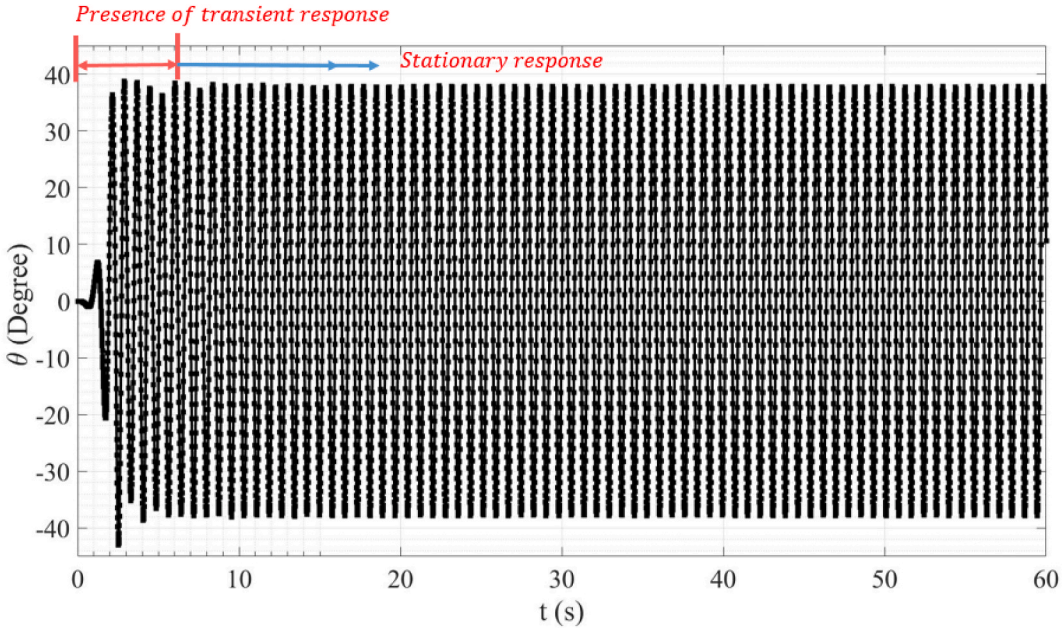

Fig. 19. Time-series response to wave period 0.78 s.

The zero-crossing analyses of the response show that the period of the first cycle is around 0.91 s (almost similar to the theoretically predicted period for the idealized mass-spring-damper system) and after 3 seconds, it continues close to 0.78 *s* with insignificant tolerance. However, the exact value of 0.78 *s* (wave period) is observed after 6 *s*; which means the other part of the response (transient) is nearly damped out after this time.

As the response is not exactly following the idealized mass-spring-damper system, and other terms are affecting the response and increase the complexity of this formula, the assumptions are numerically investigated in Section 4.2.

References

Adhikari, S., 2000. Damping Models for Structural Vibration. Eng Dep Cambridge Univ.

Ahamed, R., McKee, K., Howard, I., 2020. Advancements of wave energy converters based on power take off (PTO) systems: a review. Ocean Eng. 204, 107248. https://doi.org/10.1016/j.oceaneng.2020.107248.

Alenitsyn, A.G., Butikov, E.I., Kondratyev, A.S., 1997. Concise Handbook of Mathematics and Physics. Taylor & Francis.

Algieri Ferraro, D., Aristodemo, F., Veltri, P., 2017. Wave energy resources along calabrian coasts (Italy). In: Coastal Engineering Proceedings, p. 5. https://doi.org/10.9753/icce.v35.waves.5.

Ames, W.F., 1965. Chapter 1 the origin of nonlinear partial differential equations. In: Ames, W.F. (Ed.), Nonlinear Partial Differential Equations in Engineering, Mathematics in Science and Engineering. Elsevier, pp. 1–19. https://doi.org/10.1016/S0076-5392(08)60004-1.

Anderson, D., Tannehill, J.C., Pletcher, R.H., 2016. Computational Fluid Mechanics and Heat Transfer, Computational Fluid Mechanics and Heat Transfer, third ed. CRC Press.

Audet, C., Hare, W., 2018. Derivative-Free and Blackbox Optimization. In: Springer Series in Operations Research and Financial Engineering. Springer International Publishing.

Babarit, A., 2015. A database of capture width ratio of wave energy converters. Renew. Energy 80, 610–628. https://doi.org/10.1016/j.renene.2015.02.049.

Babarit, A., Hals, J., Muliawan, M.J., Kurniawan, A., Moan, T., Krokstad, J., 2012. Numerical benchmarking study of a selection of wave energy converters. Renew. Energy 41, 44–63. https://doi.org/10.1016/j.renene.2011.10.002.

Butikov, E.I., 1999. Parametric resonance. Comput. Sci. Eng. 1, 76–83. https://doi.org/10.1109/5992.764219.

Chakrabarti, S.K., 1987. Hydrodynamics of Offshore Structures. Computational Mechanics publication, Computational Mechanics.

Cho, Y.H., Nakamura, T., Mizutani, N., Lee, K.H., 2020. An experimental study of a bottom-hinged wave energy converter with a reflection wall in regular waves—focusing on behavioral characteristics. Appl. Sci. 10, 1–23. https://doi.org/10.3390/app10196734.

Clough, R.W., Penzien, J., 1993. Dynamics of Structures. McGraw-Hill.

Czech, B., Bauer, P., 2012. Design challenges and classification. Ieee Ind. Electron. 4–16.

Dean, R.G., Dalrymple, R.A., 1984. Water Wave Mechanics for Engineers and Scientists. https://doi.org/10.1029/eo066i024p00490-06.

Di Lauro, E., Maza, M., Lara, J.L., Losada, I.J., Contestabile, P., Vicinanza, D., 2020a. Advantages of an innovative vertical breakwater with an overtopping wave energy converter. Coast Eng. 159, 103713. https://doi.org/10.1016/j.coastaleng.2020.103713.

Di Lauro, E., Maza, M., Lara, J.L., Losada, I.J., Contestabile, P., Vicinanza, D., 2020b. Advantages of an innovative vertical breakwater with an overtopping wave energy converter. Coast Eng. 159, 103713. https://doi.org/10.1016/j.coastaleng.2020.103713.

Falcão, A.F.d.O., 2010. Wave energy utilization: a review of the technologies. Renew. Sustain. Energy Rev. 14, 899–918. https://doi.org/10.1016/j.rser.2009.11.003.

Falnes, J., 2007. A review of wave-energy extraction. Mar. Struct. 20, 185–201. https://doi.org/10.1016/j.marstruc.2007.09.001.

Faltinsen, O.M., 1990. Sea Loads on Ships & Offshore Structures_Faltinsen.Pdf. Cambridge university press.

Flick, R.E., Guza, R.T., 1980. Paddle generated waves in laboratory channels. Water way, port, coastal. Ocean Eng. 106, 79–97.

Folley, M. (Ed.), 2016. Numerical Modelling of Wave Energy Converters. Elsevier Inc. https://doi.org/10.1016/c2014-0-04006-3.

Gavin, H.P., 2016. Numerical Integration in Structural Dynamics, Numerical Integration in Structural Dynamics.

Greaves, D., Iglesias, G., 2018. Introduction, Wave and Tidal Energy. Wiley Online Books. https://doi.org/10.1002/9781119014492.ch1.

Holthuijsen, L.H., 2010. Waves in Oceanic and Coastal Waters. Cambridge University Press.

Humar, J.L., Carleton, U., 2012. Dynamics of Structures. CRC Press.

Jia, J., 2014. Essentials of Applied Dynamic Analysis. Springer.

Josh, D., Ronan, C., 2020. Efficient nonlinear hydrodynamic models for wave energy converter design-A scoping study. J. Mar. Sci. Eng. 8, 1–65. https://doi.org/10.3390/jmse8010035.

Juilfs, J., 2006. Breaking Wave Load of a Vertical Slender Cylinder within a Cylinder Group. GRIN Verlag.

Kamphuis, J.W., 2010. Introduction to Coastal Engineering and Management, Advanced Series on Ocean Engineering. World Scientific.

Karimirad, M., 2014a. Wave energy converters. In: Offshore Energy Structures: for Wind Power, Wave Energy and Hybrid Marine Platforms. Springer International Publishing, Cham, pp. 77–104. https://doi.org/10.1007/978-3-319-12175-8_5.

Karimirad, M., 2014b. Aerodynamic and hydrodynamic loads. In: Offshore Energy Structures: for Wind Power, Wave Energy and Hybrid Marine Platforms. Springer

International Publishing, Cham, pp. 187–221. https://doi.org/10.1007/978-3-319-12175-8_9.
Kusumawinahyu, W.M., Karjanto, N., Klopman, G., 2017. Linear Theory for Single and Double Flap Wavemakers.
Lee, C.-H., 1995. WAMIT Theory Manual. WAMIT, Inc. Massachusetts Institute of Technology.
López, I., Andreu, J., Ceballos, S., Martínez De Alegría, I., Kortabarria, I., 2013. Review of wave energy technologies and the necessary power-equipment. Renew. Sustain. Energy Rev. 27, 413–434. https://doi.org/10.1016/j.rser.2013.07.009.
Ma, Q., 2010. Advances in numerical simulation of nonlinear water waves. In: Advances in Coastal and Ocean Engineering. World Scientific.
Marco, Alves, 2017. Handbook of Ocean Wave Energy- Wave-To-Wire Modelling of WECs, Ocean Engineering & Oceanography. Springer International Publishing.
[WWW Document] Matlab, 2019. www.mathworks.com.
Mei, C., 2012. Hydrodynamic principles of wave power extraction. Philos. Trans. A Math. Phys. Eng. Sci. 370, 208–234. https://doi.org/10.1098/rsta.2011.0178.
Mei, C., Stiassnie, M., Yue, D., 2005. Theory and Applications of Ocean Surface Waves. Part I: Linear Aspects. World Scientific.
Mendoza, E., Silva, R., Zanuttigh, B., Angelelli, E., Lykke Andersen, T., Martinelli, L., Nørgaard, J.Q.H., Ruol, P., 2014. Beach response to wave energy converter farms acting as coastal defence. Coast Eng. 87, 97–111. https://doi.org/10.1016/j.coastaleng.2013.10.018.
Michele, S., Sammarco, P., D'Errico, M., 2016. The optimal design of a flap gate array in front of a straight vertical wall: resonance of the natural modes and enhancement of the exciting torque. Ocean Eng. 118, 152–164. https://doi.org/10.1016/j.oceaneng.2016.04.002.
MIT, 2005. Wave Forces on a Body, Marine Hydrodynamics Lectures.
Navionics, 2021. Water depth [WWW Document]. URL. https://webapp.navionics.com/.
Nayfeh, A.H., Mook, D.T., 1979. Nonlinear Oscillations, Pure and Applied Mathematics: A Wiley Series of Texts, Monographs and Tracts. Wiley.
Nolte, J.D., Ertekin, R.C., 2014. Wave power calculations for a wave energy conversion device connected to a drogue. J. Renew. Sustain. Energy 6. https://doi.org/10.1063/1.4862785.
Pecher, A., 2017. In: Pecher, A., Kofoed, J.P. (Eds.), Experimental Testing and Evaluation of WECs BT - Handbook of Ocean Wave Energy. Springer International Publishing, Cham, pp. 221–260. https://doi.org/10.1007/978-3-319-39889-1_9.
Pecher, A., Costello, R., 2017. In: Pecher, A., Kofoed, J.P. (Eds.), Techno-Economic Development of WECs BT - Handbook of Ocean Wave Energy. Springer International Publishing, Cham, pp. 81–100. https://doi.org/10.1007/978-3-319-39889-1_4.
Pecher, A., Kofoed, J.P., 2017. Introduction. In: Pecher, A., Kofoed, J.P. (Eds.), Handbook of Ocean Wave Energy. Springer International Publishing, Cham, pp. 1–15. https://doi.org/10.1007/978-3-319-39889-1_1.
Qiao, D., Haider, R., Yan, J., Ning, D., Li, B., 2020. Review of wave energy converter and design of mooring system. Sustain. Times 12, 1–31. https://doi.org/10.3390/su12198251.
Renzi, E., Abdolali, A., B, G., Dias, F., 2012. Mathematical modelling of the oscillating wave surge converter. In: XXXIII Convegno Nazionale Di Idraulica e Costruzioni Idrauliche.
Rodríguez, C.A., Rosa-Santos, P., Taveira-Pinto, F., 2019. Assessment of damping coefficients of power take-off systems of wave energy converters: a hybrid approach. Energy 169, 1022–1038. https://doi.org/10.1016/j.energy.2018.12.081.
Rosa-Santos, P., Taveira-Pinto, F., Clemente, D., Cabral, T., Fiorentin, F., Belga, F., Morais, T., 2019. Experimental study of a hybrid wave energy converter integrated in a harbor breakwater. J. Mar. Sci. Eng. 7, 1–18. https://doi.org/10.3390/jmse7020033.
Ruehl, K., Forbush, D.D., Yu, Y.H., Tom, N., 2020. Experimental and numerical comparisons of a dual-flap floating oscillating surge wave energy converter in regular waves. Ocean Eng. 196, 106575. https://doi.org/10.1016/j.oceaneng.2019.106575.
Saeidtehrani, S., 2015. Physical and Numerical Modeling of a Wave Energy Converter. Roma Tre University.
Saeidtehrani, S., Lomonaco, P., Hagmuller, A., Levites-ginsburg, M., 27 . Application of a simulation model for a heave type wave energy converter. In: Lewis, A. (Ed.), Proceedings of the Twelfth European Wave and Tidal Energy Conference. EWTEC, 948-1–948–8. ISSN: 2309-1983.
Sammarco, P., Tran, H.H., Mei, C.C., 1997. Subharmonic resonance of Venice gates in waves. Part 1. Evolution equation and uniform incident waves. J. Fluid Mech. 349, 295–325. https://doi.org/10.1017/S0022112097006848.
Sammarco, P., Michele, S., D'Errico, M., 2015. Il cassone syncres: assorbimento del moto ondoso e generazione di energia elettrica. Rome, Italy.
Sammarco, P., Michele, S., d'Errico, M., Bellotti, G., 2016. IL CASSONE SYNC. RE.S.
Sorensen, R.M., 2006. Basic Coastal Engineering: Third Edition, Basic Coastal Engineering, third ed. https://doi.org/10.1007/b101261
Svendsen, I.A., 2006. Introduction to Nearshore Hydrodynamics, Advanced Series on Ocean Engineering.
Têtu, A., 2017. Handbook of Ocean Wave Energy- Power Take-Off Systems for WECs. Springer International Publishing. https://doi.org/10.1007/978-3-319-39889-1_8.
Todalshaug, J.H., 2017. In: Pecher, A., Kofoed, J.P. (Eds.), Hydrodynamics of WECs - Handbook of Ocean Wave Energy. Springer International Publishing, Cham, pp. 139–158. https://doi.org/10.1007/978-3-319-39889-1_6.
Uihlein, A., Magagna, D., 2016. Wave and tidal current energy - a review of the current state of research beyond technology. Renew. Sustain. Energy Rev. 58, 1070–1081. https://doi.org/10.1016/j.rser.2015.12.284.
Zanuttigh, B., Angelelli, E., 2013. Experimental investigation of floating wave energy converters for coastal protection purpose. Coast Eng. 80, 148–159. https://doi.org/10.1016/j.coastaleng.2012.11.007.
Zhao, X.L., Ning, D.Z., Zou, Q.P., Qiao, D.S., Cai, S.Q., 2019. Hybrid floating breakwater-WEC system: a review. Ocean Eng. 186, 106126. https://doi.org/10.1016/j.oceaneng.2019.106126.